Applied Physics Letters

RESEARCH ARTICLE | MARCH 14 2023

Impact of minor hysteresis loops in integrated inductors with ferromagnetic films

S. Cuccurullo ; F. Maspero ; O. Koplak ; G. Pavese ; E. Albisetti ; M. Cantoni ; R. Bertacco

Appl. Phys. Lett. 122, 113503 (2023)
https://doi.org/10.1063/5.0127390

Applied Physics Letters ARTICLE scitation.org/journal/apl

Impact of minor hysteresis loops in integrated inductors with ferromagnetic films

Cite as: Appl. Phys. Lett. **122**, 113503 (2023); doi: 10.1063/5.0127390
Submitted: 21 September 2022 · Accepted: 1 March 2023 ·
Published Online: 14 March 2023

S. Cuccurullo,[1,a)] F. Maspero,[2] O. Koplak,[1] G. Pavese,[1] E. Albisetti,[1] M. Cantoni,[1] and R. Bertacco[1]

AFFILIATIONS

[1]Department of Physics, Politecnico di Milano, Milan, Italy
[2]Department of Civil and Environmental Engineering, Politecnico di Milano, Milan, Italy

[a)]Author to whom correspondence should be addressed: simone.cuccurullo@polimi.it

ABSTRACT

Integration of inductors on silicon chips is becoming more and more relevant for monolithic electronic applications. In this Letter, we investigate the impact of minor hysteresis loops in an integrated inductor with spiral geometry sandwiched between two soft magnetic layers made of MoNiFe/Cr multilayers. Despite high magnetic susceptibility and low coercivity of optimized multilayers, we find that the inductance is strongly dependent on the AC voltage applied to the device, showing a bell-shaped behavior. Comparing the measured inductance with magneto-optical Kerr effect and vibrating sample magnetometry measurements, we show that the low-signal behavior is limited by domain wall pinning/depinning, which determine the effective susceptibility associated with minor hysteresis loops driven by the applied AC voltage.

Monolithic solutions for wireless communications, RF circuits, and power electronics nowadays require the integration of inductors on the silicon chip. In the last two decades, several groups proposed the addition of a magnetic material to the inductor to find the best compromise between device performance and on-chip area; indeed, similarly to macroscopic devices, magnetic materials allow larger stored magnetic energy, leading to an enhancement of the inductance without the need of increasing the size of the device. Examples of the proposed geometries comprise planar structures, like spiral and meander inductors sandwiched between two magnetic films,[1] and 3D structures, like solenoids and toroids with magnetic film cores.[2,3] More recent advances in the field[4] have shown the effectiveness of newly developed technologies, e.g., on-chip intercalated graphene inductors,[5] self-rolled-up membranes,[6] and 3D-printed polymer/metal micro-coils,[7] and some of them also include magnetic cores. However, the integration of on-chip inductors and magnetic films comes with several issues such as: (i) process compatibility,[8] (ii) magnetic core saturation at high bias currents,[9] and (iii) losses due to eddy currents and hysteresis loops.[10] In particular, the impact of the hysteresis of magnetic materials is important in applications in which the inductor is excited with strong AC, e.g., in DC–DC or in resonant converters.[11] In this case, the small signal impedance characterization is not sufficient to describe the behavior of the device in its working regime; instead, a large signal analysis is required. So far, many studies have been focusing on the small signal behavior of integrated inductors,[1,11–13] while a comprehensive analysis of the connection between the magnetic properties of the embedded ferromagnetic elements and their large signal impedance is still missing.

In this Letter, we study the impact of minor hysteresis loops on the large signal impedance of an inductor exploiting the confinement of the magnetic field within soft ferromagnetic layers, fabricated on a silicon chip using wafer-scale planar technology. As reported in Fig. 1(a), we chose a spiral geometry for the inductor, which is well-suited for the integration in a planar process. The inductor is sandwiched between two magnetic films and electrically isolated from them by means of two insulating layers.

The addition of magnetic films with high relative permeability allows one to concentrate, inside the magnetic volume, the field produced by current I flowing in the inductor; this way, the stored magnetic energy increases and so does the inductance. This effect is evident in the simulation (COMSOL Multiphysics[14]) of field lines reported in Fig. 1(b), which reports a lateral view of a region of the device and shows an effective confinement except for the inductor edges. Moreover, as we shown in Fig. 1(c), for high values of the permeability μ_r, compatible with our experiments, the demagnetizing field inside the material smoothens out the spatial oscillating behavior of the field produced by the spiral winding.

Devices were fabricated using Cu as a conductive material, polyimide (PI 2610, HD MicroSystems) as an insulating layer, and the ternary alloy molybdenum-permalloy ($Mo_5Ni_{75}Fe_{20}$) as a magnetic material.

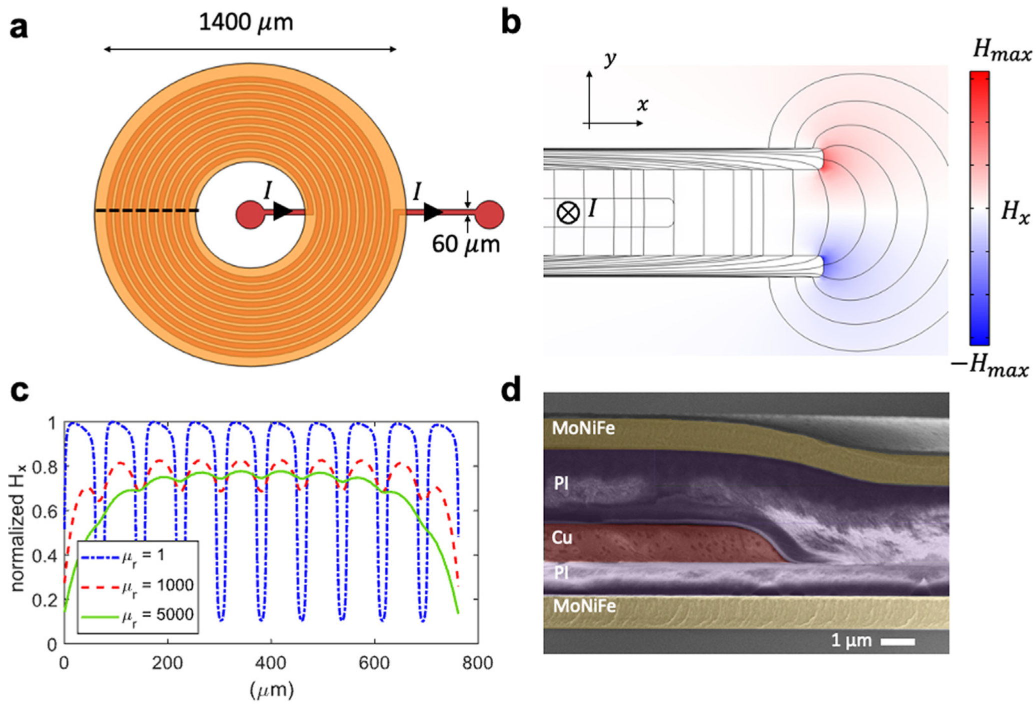

FIG. 1. (a) Top-view of the designed spiral inductor (in red) sandwiched between two magnetic layers (in orange); *I* is the current injected in the device. (b) Simulated field lines of the *H* field at the edge of the structure; the color-plot refers to the *x* component of the *H* field. (c) Simulated in-plane H_x field profiles in the magnetic material along the dashed line of panel (a). (d) False-color SEM cross section of the edge of a device.

Even though other alloys, like CoZrTa,[8] display superior properties at high frequencies (lower losses due to smaller coercivity and eddy currents), here we consider an alloy of the NiFe family, which provides higher values of permeability and can be suitable for low frequency applications. Note, however, that the physical phenomenon investigated in this paper is independent of the specific magnetic material used in the core.

For each patterning step, we employed standard optical lithography with the AZ nLOF 2070 photoresist (MicroChemicals GmbH). The process steps are: (i) Si substrate cleaning, (ii) RF sputter deposition of the bottom magnetic layer, (iii) PI deposition and curing at 300 °C, (iv) Cu RF sputter deposition, with Cr as an adhesion layer, (v) PI deposition and curing, (vi) RF sputter deposition of the top magnetic layer, and (vii) reactive-ion etching in O_2 plasma to selectively etch PI over electric contacts. In Fig. 1(d), we report a scanning electron microscope (SEM) cross section of a device.

To maximize the inductance, a careful optimization of the soft magnetic layer has been carried out to obtain high permeability and low coercivity.

It is well-known that, above a critical thickness, some magnetic films (e.g., Co,[15,16] NiFe[17,18]) show a transition from an in-plane (IP) anisotropy to an out-of-plane (OOP) one with formation of alternating adjacent magnetic domains, called stripe domains (SDs). Either the columnar structure of the polycrystalline film or its residual stress promotes the transition.[19] When the film thickness is larger than the critical thickness, the perpendicular magnetization of the SDs lowers the permeability and increases both the saturation field and the coercivity, thus making them unsuitable for integrated inductors. Note that the presence of SDs involves also an anomalous behavior in magnetization dynamics, which is observed at high frequencies[20] and could introduce additional non-idealities in the inductor performances.

One way to overcome the issue of SDs is to use a multilayer with non-magnetic spacers.[21,22] Indeed, a multilayer allows us to obtain a large magnetic volume, still keeping the thickness of the single magnetic layer below the critical value. In this work, we employed a Cr/MoNiFe multilayer. To estimate the critical thickness, we deposited the multilayers [Cr (5 nm)/MoNiFe (640/n nm)]$_n$ by RF sputtering with $n = 1$, 4, and 8. The corresponding MoNiFe thicknesses of the single magnetic layer (t_s) are 640, 160, and 80 nm to maintain the total magnetic volume constant. We characterized the multilayers by vibrating sample magnetometry (VSM), magnetic force microscopy (MFM), and SEM. As it is evident from the MFM images of Fig. 2, SDs appear for t_s = 160 and 640 nm. Indeed, in-plane hysteresis loops by VSM show relatively large coercivity and large saturation field. In contrast, for t_s = 80 nm, the multilayer does not show SDs and presents a narrower hysteresis loop; the estimated permeability and coercive field are around 6000 and 0.5 Oe, respectively. Note that the state of the art 100 nm thick CoZrTa shows lower permeability (around 1000) and lower coercivity (0.015 Oe).[8] Considering the SEM images, we believe that columnar shape anisotropy is responsible for the formation of the OOP anisotropy. Indeed, the cross sections of the samples with t_s = 640 and 160 nm show columnar features, which are not present in the case of t_s = 80 nm. Given its better performance, we adopted the [Cr (5 nm)/MoNiFe (80 nm)]$_8$ multilayer for the integrated planar inductor.

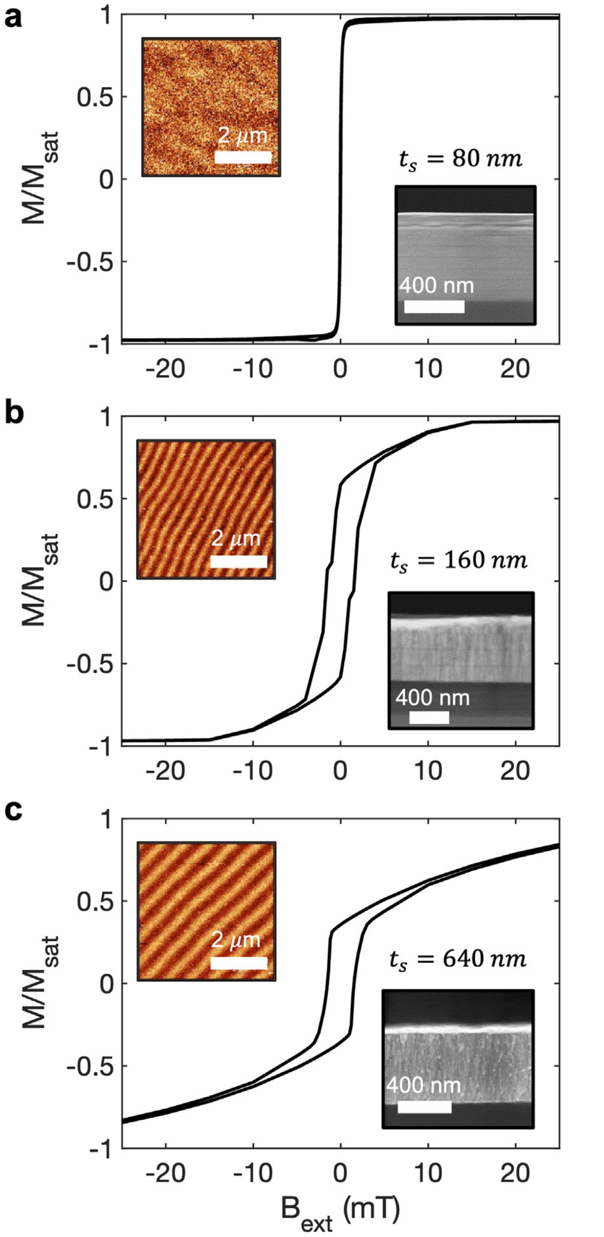

FIG. 2. MFM images (top-left inset), in-plane VSM loop (main plot), and SEM cross sections (bottom-right inset) for (a) [Cr (5 nm)/MoNiFe (80 nm)]$_8$, (b) [Cr (5 nm)/MoNiFe (160 nm)]$_4$, and (c) Cr (5 nm)/MoNiFe (640 nm). For every film, the value of the saturation magnetization is $\mu_0 M_{sat} = 0.80 \pm 0.03$ T.

We did not investigate thicknesses below the critical value of 80 nm, because a further decrease in the single layer thickness could lead to an increase in the coercive field and a shift of the loop due to enhanced Néel coupling arising from interfacial roughness.[23] Moreover, we wanted to keep the fabrication process as simple as possible.

Electrical measurements were carried out with a Keysight E4980A LCR meter. To characterize the device, we employed both an AC voltage source to extract the complex impedance and a DC source to superimpose a bias current. Data reported here were taken at 10 kHz, which is low enough to avoid major effects due to LC resonance and eddy currents in the magnetic layer.[8] In this condition, we can safely model the device as a resistor and an inductor in series. The inductance is then extracted from the imaginary part of the complex impedance measured by the instrument.

First, we characterized the inductance L as a function of the DC bias current I_{bias} for different rms values of the AC voltage V_{ac} [see Fig. 3(a)]. The curves show the same behavior: the inductance is constant up to a certain I^* and then decreases. This effect is due to the saturation of the magnetic films; indeed, when I_{bias} increases, also the static field generated by the conductive coil increases. When the magnetic film enters the saturation region, the permeability drops and the inductance decreases. Noteworthy, I^* is smaller for larger V_{ac}, as the saturation condition is reached earlier for large values of the AC field. Moreover, also for small I_{bias}, i.e., far away from saturation, we observe

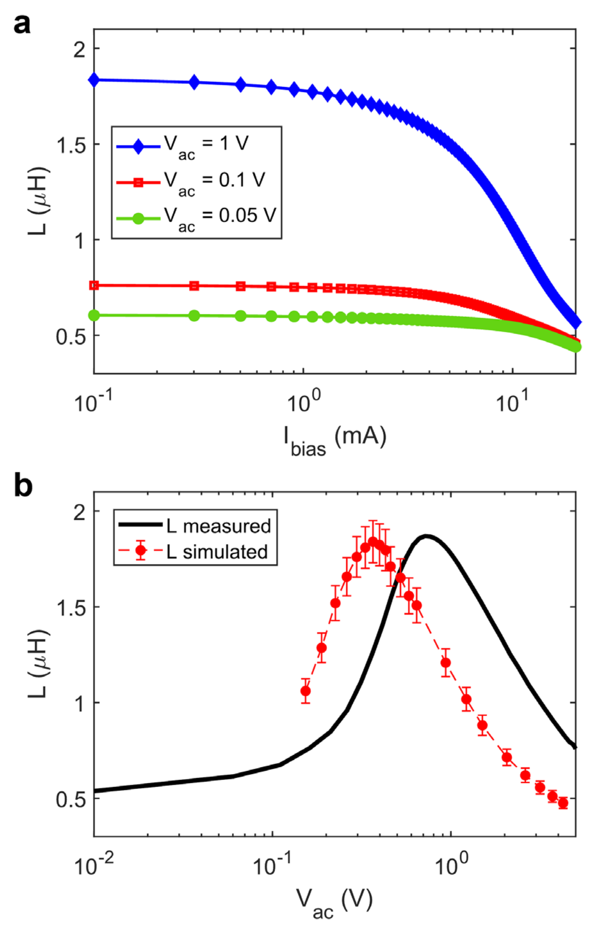

FIG. 3. (a) Measured inductance at 10 kHz as a function of the bias current I_{bias} for different values of the AC voltage rms V_{ac}. (b) Solid black line: measured inductance as a function of V_{ac} with $I_{bias} = 0$. Dashed red line: simulated inductance for the values of permeability extracted from major and minor hysteresis loops [Fig. 4(b)]; error bars are due to the uncertainty on (i) the saturation magnetization of the magnetic multilayer and (ii) the geometrical parameters of the fabricated inductor.

sizable variations of inductance for different values of the AC voltage amplitude. To understand this effect, we studied in more detail the inductance as a function of the V_{ac} with no bias current applied ($I_{bias} = 0$). As reported in Fig. 3(b), the measured inductance (solid black line) is almost constant for small values of the AC amplitude. As V_{ac} increases, entering in the large signal regime, L increases until it reaches a peak value, and then it drops. This behavior was already observed in the large signal analysis of integrated inductors with ferromagnetic core.[11,24] The authors justified the results by considering the impact of the nonlinear magnetization curve of the core material without elaborating on the effect further.

Here, we show that the origin of this effect is related to different features of minor and major hysteresis loops of the magnetic material. To this scope, we recorded minor loops from our magnetic multilayer by using complementary techniques. First, we performed longitudinal magneto-optical Kerr effect (MOKE) measurements to investigate the local effect of magnetic domain wall motion on minor hysteresis loops. The goal of the measurement is to understand how the amplitude of an AC magnetic field affects the hysteresis of the material and, subsequently, exploit this information to justify the behavior of the inductance as a function of the AC voltage amplitude. During the MOKE measurements, a low-frequency (10 Hz) magnetic field was applied in-plane to the multilayer; each minor loop reported in Fig. 4(a) corresponds to a different AC field amplitude (from left to right: 0.4, 0.6, 0.9, and 1 Oe). If the latter is sufficiently small, we do not observe evident Barkhausen jumps [first two graphs of Fig. 4(a) starting from the left]. In this regime, the response of the material is weak, because magnetic domain walls are pinned and the bulging of walls dominates the magnetization process.[25] Note that this regime is favored by additional pinning sites introduced by each interface in the multilayer. In contrast, for larger AC amplitudes, Barkhausen jumps appear [last two graphs of Fig. 4(a)]; domain walls unpin and displace, leading to a stronger response of the magnetization with respect to the applied field.

MOKE measurements point to the existence of two regimes: for low AC amplitudes, the material shows a weak response to the external field, therefore its susceptibility, estimated from the slope of a linear fit of the whole loop, is almost constant; for higher AC amplitudes, due to the depinning of domain walls, the effective susceptibility χ_{eff} increases as the amplitude increases. Considering this, we can explain the dependence of the inductance on the AC voltage reported in the electrical measurement of Fig. 3(b). Since the inductance is proportional to the effective permeability $\mu_{r,eff}$ of the magnetic material, it is almost constant for low AC amplitudes of the applied voltage, i.e., for low AC amplitudes of the field generated by the conductive coil. As the amplitude increases, domain walls unpin and displace, leading to a larger permeability, thus a larger inductance. After reaching a peak value, the inductance drops because of the saturation of the material, which leads to a decrease in the permeability.

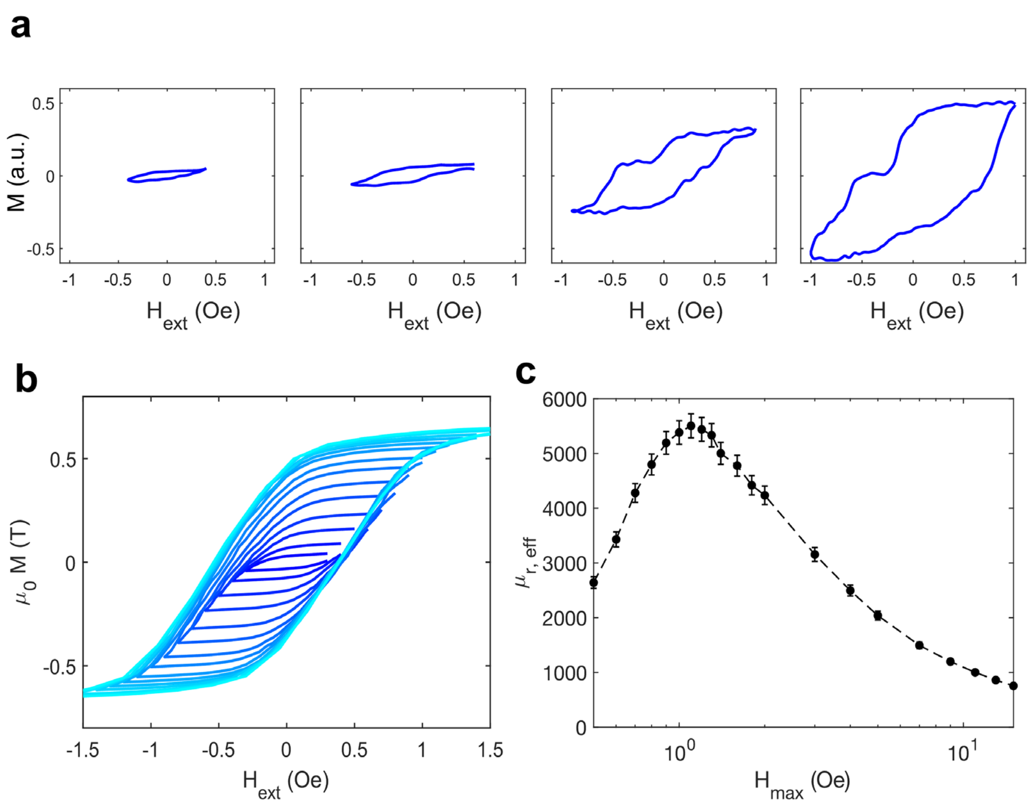

FIG. 4. (a) Minor hysteresis loops obtained through MOKE measurements on the magnetic multilayer. (b) Minor and major hysteresis loops of the magnetic multilayer measured by VSM. (c) Effective relative permeability extracted from the VSM hysteresis loops; error bars are due to the uncertainty on the saturation magnetization value.

To put these considerations on a more quantitative basis, we performed quasi-static VSM measurements on the magnetic multilayer to obtain accurate minor and major hysteresis loops and extract the effective susceptibility, hence, permeability, for each of them. At variance with MOKE, in VSM measurements, the effect of Barkhasuen jumps is averaged out over the whole sample. This situation is more similar to the integrated inductor working condition, where the whole multilayer determines the effective permeability and the inductance.

In Fig. 4(b), we report minor and major hysteresis loops measured by VSM. For each of them, we swept quasi-statically the external field from H_{max} to $-H_{max}$ and then back to H_{max}. To extract the effective susceptibility χ_{eff}, we performed a linear fitting of each loop to evaluate the average derivative of the magnetization M with respect to the external field H_{ext}. Assuming the validity of the relation $\mu_{r,eff} = \chi_{eff} + 1$, where $\mu_{r,eff}$ is the effective relative permeability, we obtained $\mu_{r,eff}$ as a function of H_{max}, which is plotted in Fig. 4(c). Noteworthy, we find a peak mimicking that of the large signal inductance vs V_{ac} in Fig. 3(b). Note that, due to the limited resolution of the VSM field source, we could not reach smaller values of H_{max}; therefore, we could not measure the plateau on the left side of the peak of the permeability for small values of the applied field.

For direct comparison with experimental data on the large signal inductance, a correlation between the field amplitude (H_{max}) used for minor loops measurements with VSM and V_{ac} is needed. To this scope, we performed FEM simulations on COMSOL Multiphysics [see Fig. 1(c)]. First, we assumed a linear magnetic material and run a simulation for all the values of the effective permeability $\mu_{r,eff}$ from VSM measurements. For each value of the permeability, the conversion factor between H_{max} and the AC voltage rms value V_{ac} was obtained, considering the average in-plane H field generated in the magnetic volume per unit voltage applied to the device. From the same simulation, we then extracted the inductance for each value of $\mu_{r,eff}$ and associated it to the proper V_{ac} using the conversion factor described above. The resulting curve for the simulated large signal inductance is plotted in Fig. 3(b) on the same graph of the electrically measured inductance. The curves have the same shape, and the values of the inductance also match; however, they are shifted one respect to the other. We believe that the shift could be caused by magnetic relaxation phenomena affecting hysteresis loops at different frequencies.[26] Since the inductance is measured at 10 kHz, while the VSM measurements are quasi-static, the effective permeability estimated from VSM minor loops could be higher than that at high frequencies determining the inductance due to magnetic relaxation. Furthermore, the shift could be due to the different geometries of the inductor and of the VSM measurements; indeed, the conductive coil of the inductor produces a field with cylindrical symmetry, while the field applied by the electromagnet during VSM measurement is uniform on the sample volume. This could lead to spurious contributions that affect the conversion factor employed to plot the simulated curve.

To summarize, in this Letter, we investigated the impact of minor hysteresis loops in integrated inductors exploiting ferromagnetic films. We show that the effect of minor loops on the large signal analysis of the device is critical even if a high-permeability magnetic material is employed. For an integrated inductor made of a Cu spiral and sandwiched between two MoNiFe/Cr multilayers, the large signal inductance peaks at a specific value of the applied voltage signal. For lower signal amplitudes, the shape of minor loops limits the effective permeability, while for higher amplitudes, the saturation of the magnetic films is the cause of the inductance decrease. Complementary MOKE and VSM analyses show that the limiting factor for the effective susceptibility associated with minor loops is connected to domain wall pinning/depinning. This work sheds light on the physical origin of the dependency of large signal inductance on the signal amplitude, indicating that the optimization of the inductor performance requires careful engineering of the magnetic layer. In the first place, the impact of the effect can be reduced in magnetic materials with lower coercivity. For example, CoZrTa multilayers display a smaller coercivity,[8] so that the impact of minor loops is expected to be reduced. In the second place, the growth conditions can be optimized to reduce the density of pinning sites for domain walls. Finally, the material could be patterned to promote the propagation of walls in guiding structures. All these strategies can be adopted to minimize the impact of minor loops and improve the linearity of inductors with magnetic core.

This work was supported by the Joint Research Centre MEMS Lab and STEAM between Politecnico di Milano and STMicroelectronics. The research leading to these results has received funding from the European Research Council (ERC) under the European Union's Horizon 2020 Research and Innovation Program (Grant Agreement No. 948225). The authors acknowledge the availability of experimental facilities at PoliFAB, the Micro- and Nanotechnology Center of the Politecnico di Milano.

AUTHOR DECLARATIONS

Conflict of Interest

The authors have no conflicts to disclose.

Author Contributions

Simone Cuccurullo: Conceptualization (equal); Data curation (lead); Formal analysis (lead); Investigation (lead); Methodology (equal); Project administration (equal); Software (lead); Validation (lead); Visualization (lead); Writing – original draft (lead); Writing – review & editing (equal). **Federico Maspero:** Conceptualization (equal); Data curation (supporting); Formal analysis (supporting); Investigation (equal); Methodology (equal); Project administration (equal); Software (supporting); Supervision (equal); Validation (supporting); Visualization (supporting); Writing – review & editing (equal). **Oksana Koplak:** Investigation (equal); Resources (equal); Software (equal); Validation (equal); Visualization (equal). **Giulia Pavese:** Investigation (equal); Visualization (equal). **Edoardo Albisetti:** Investigation (equal); Resources (equal); Visualization (equal); Writing – review & editing (equal). **Matteo Cantoni:** Investigation (equal); Resources (equal); Software (equal); Visualization (equal); Writing – review & editing (equal). **Riccardo Bertacco:** Conceptualization (equal); Data curation (supporting); Formal analysis (supporting); Funding acquisition (lead); Investigation (equal); Methodology (equal); Project administration (equal); Resources (equal); Supervision (equal); Visualization (supporting); Writing – review & editing (equal).

DATA AVAILABILITY

The data that support the findings of this study are available from the corresponding author upon reasonable request.

REFERENCES

[1]D. V. Harburg, A. J. Hanson, J. Qiu, B. A. Reese, J. D. Ranson, D. M. Otten, C. G. Levey, and C. R. Sullivan, "Microfabricated racetrack inductors with thin-film magnetic cores for on-chip power conversion," IEEE J. Emerging Sel. Top. Power Electron. **6**, 1280–1294 (2018).
[2]D. W. Lee, K.-P. Hwang, and S. X. Wang, "Fabrication and analysis of high-performance integrated solenoid inductor with magnetic core," IEEE Trans. Magn. **44**, 4089–4095 (2008).
[3]F. Hettstedt, U. Schürmann, R. Knöchel, and E. Quandt, "Toroid microinductors using segmented magnetic cores," in *2010 IEEE MTT-S International Microwave Symposium* (IEEE, 2010), pp. 1348–1351.
[4]H. T. Le, R. I. Haque, Z. Ouyang, S. W. Lee, S. I. Fried, D. Zhao, M. Qiu, and A. Han, "MEMS inductor fabrication and emerging applications in power electronics and neurotechnologies," Microsyst. Nanoeng. **7**, 59 (2021).
[5]J. Kang, Y. Matsumoto, X. Li, J. Jiang, X. Xie, K. Kawamoto, M. Kenmoku, J. H. Chu, W. Liu, J. Mao *et al.*, "On-chip intercalated-graphene inductors for next-generation radio frequency electronics," Nat. Electron. **1**, 46–51 (2018).
[6]W. Huang, Z. Yang, M. D. Kraman, Q. Wang, Z. Ou, M. M. Rojo, A. S. Yalamarthy, V. Chen, F. Lian, J. H. Ni *et al.*, "Monolithic MTesla-level magnetic induction by self-rolled-up membrane technology," Sci. Adv. **6**, eaay4508 (2020).
[7]C. W. Ha, P. Prabhakaran, and Y. Son, "3D-printed polymer/metal hybrid microstructures with ultraprecision for 3D microcoils," 3D Printing Addit. Manuf. **6**, 165–170 (2019).
[8]D. S. Gardner, G. Schrom, F. Paillet, B. Jamieson, T. Karnik, and S. Borkar, "Review of on-chip inductor structures with magnetic films," IEEE Trans. Magn. **45**, 4760–4766 (2009).
[9]N. Wang, T. O'Donnell, R. Meere, F. M. Rhen, S. Roy, and S. C. O'Mathuna, "Thin-film-integrated power inductor on Si and its performance in an 8-MHz buck converter," IEEE Trans. Magn. **44**, 4096–4099 (2008).
[10]R. Meere, N. Wang, T. O'Donnell, S. Kulkarni, S. Roy, and S. C. O'Mathuna, "Magnetic-core and air-core inductors on silicon: A performance comparison up to 100 MHz," IEEE Trans. Magn. **47**, 4429–4432 (2011).
[11]Y. Fukuda, T. Inoue, T. Mizoguchi, S. Yatabe, and Y. Tachi, "Planar inductor with ferrite layers for DC-DC converter," IEEE Trans. Magn. **39**, 2057–2061 (2003).
[12]L. Milner and G. A. Rincón-Mora, "Small saturating inductors for more compact switching power supplies," IEEE. Trans. Electr. Electron. Eng. **7**, 69–73 (2012).
[13]J. Kaiser and T. Dürbaum, "An overview of saturable inductors: Applications to power supplies," IEEE Trans. Power Electron. **36**, 10766–10775 (2021).
[14]C. Multiphysics, *Introduction to COMSOL Multiphysics*®, COMSOL Multiphysics, Burlington, MA, 1998, accessed on February 9, 2018.
[15]M. Hehn, S. Padovani, K. Ounadjela, and J. Bucher, "Nanoscale magnetic domain structures in epitaxial cobalt films," Phys. Rev. B **54**, 3428 (1996).
[16]C. Hsieh, J. Liu, and J. Lue, "Magnetic force microscopy studies of domain walls in nickel and cobalt films," Appl. Surf. Sci. **252**, 1899–1909 (2005).
[17]N. Saito, H. Fujiwara, and Y. Sugita, "A new type of magnetic domain structure in negative magnetostriction Ni-Fe films," J. Phys. Soc. Jpn. **19**, 1116–1125 (1964).
[18]R. J. Spain, "Stripe domains in nickel/iron films," Appl. Phys. Lett. **6**, 8–9 (1965).
[19]D. Lo and M. Hanson, "Origin of stripe domains in Ni–Fe films," J. Appl. Phys. **38**, 1342–1343 (1967).
[20]W. Tee Soh, N. N. Phuoc, C. Tan, and C. Ong, "Magnetization dynamics in permalloy films with stripe domains," J. Appl. Phys. **114**, 053908 (2013).
[21]S. Cheng, P. Lubitz, Y. Zheng, and A. Edelstein, "Effects of spacer layer on growth, stress and magnetic properties of sputtered permalloy film," J. Magn. Mag. Mater. **282**, 109–114 (2004).
[22]T. Dastagir, W. Xu, S. Sinha, H. Wu, Y. Cao, and H. Yu, "Tuning the permeability of permalloy films for on-chip inductor applications," Appl. Phys. Lett. **97**, 162506 (2010).
[23]A. T. Nguyen, T. L. Nguyen, A. T. Nguyen, Q. K. Hoang *et al.*, "Enhanced soft magnetic properties of [NiFe/Ta]n laminated films for flux amplification in magnetic sensors," IEEE Trans. Magn. **54**, 1–4 (2018).
[24]T. Sato, K. Yamasawa, H. Tomita, T. Inoue, and T. Mizoguchi, "FeCoBn magnetic thin film inductor for MHz switching micro DC-DC converters," IEEJ Trans. Ind. Appl. **121**, 84–89 (2001).
[25]R. Valenzuela, "Low-frequency magnetoimpedance: Domain wall magnetization processes," Phys. B: Condens. Matter **299**, 280–285 (2001).
[26]C. Nistor, E. Faraggi, and J. Erskine, "Magnetic energy loss in permalloy thin films and microstructures," Phys. Rev. B **72**, 014404 (2005).